

# Discovery of X-ray Pulsation from the Geminga-like Pulsar PSR J2021+4026

L. C. C. Lin<sup>1</sup>, C. Y. Hui<sup>2</sup>, C. P. Hu<sup>3</sup>, J. H. K. Wu<sup>4</sup>, R. H. H. Huang<sup>4</sup>, L. Trepl<sup>5</sup>, J. Takata<sup>6</sup>,  
K. A. Seo<sup>2</sup>, Y. Wang<sup>6</sup>, Y. Chou<sup>3</sup> and K. S. Cheng<sup>6</sup>

cyhui@cnu.ac.kr

## ABSTRACT

We report the discovery of X-ray periodicity of  $\sim 265.3$  ms from a deep *XMM-Newton* observation of the radio-quiet  $\gamma$ -ray pulsar, PSR J2021+4026, located at the edge of the supernova remnant G78.2+2.1 ( $\gamma$ -Cygni). The detected frequency is consistent with the  $\gamma$ -ray pulsation determined by the observation of *Fermi* Gamma-ray Space Telescope at the same epoch. The X-ray pulse profile resembles the modulation of hot spot on the surface of the neutron star. The phase-averaged spectral analysis also suggests that the majority of the observed X-rays have a thermal origin. This is the *third* member in the class of radio-quiet pulsars with the significant pulsations detected from both X-rays and  $\gamma$ -ray regimes.

*Subject headings:* Gamma rays: general — pulsars: general — ISM: individual objects: G78.2+2.1 — pulsars: individual (PSR J2021+4026) — X-rays: general — radiation mechanisms: thermal

## 1. Introduction

Before the launch of *Fermi* Gamma-ray Space Telescope, there was only one radio-quiet  $\gamma$ -ray pulsar has been known, namely Geminga (i.e. PSR B0633+17 Bertsch et al. 1992).

---

<sup>1</sup>General Education Center, China Medical University, Taichung 40402, Taiwan

<sup>2</sup>Department of Astronomy and Space Science, Chungnam National University, Daejeon, South Korea

<sup>3</sup>Graduate Institute of Astronomy, National Central University, Jhongli 32001, Taiwan

<sup>4</sup>Institute of Astronomy, National Tsing-Hua University, Hsinchu 30013, Taiwan

<sup>5</sup>Astrophysikalisches Institut and Universitäts-Sternwarte, Universität Jena, Schillergäßchen 2-3, 07745 Jena, Germany

<sup>6</sup>Department of Physics, University of Hong Kong, Pokfulam Road, Hong Kong, PRC

The high sensitivity of Large Area Telescope (LAT) on board *Fermi* enables an efficient search of  $\gamma$ -ray pulsars (Abdo et al. 2008, 2010a; Ackermann et al. 2011). Soon after the commence of the mission, (Abdo et al. 2009a) has reported the detections of 16 pulsars with 13 of them remain to be radio-quiet after the dedicated radio pulsation search (Camilo et al. 2009; Abdo et al. 2010b). The population of radio-quiet  $\gamma$ -ray pulsars has been expanded to 22 based on the extensive searches of Saz Parkinson et al. (2010). Thanks to the improved search techniques provided by Kerr (2011) & Pletsch (2011), in total, there are 31 radio-quiet  $\gamma$ -ray pulsars are currently known (Pletsch et al. 2012a,b).

For this class of pulsars, the lack of knowledge in the phase relationship between the  $\gamma$ -ray light curve and that in radio leads to an ambiguity in investigating their emission region and physical processes (see the discussion in Trepl et al. 2010). Therefore, pulsation searches in the other frequencies are fundamentally important for a better understanding to the physics of this class of pulsars. So far, there are only Geminga (Halpern & Holt 1992) and PSR J0007+7303 (Lin et al. 2010; Caraveo et al. 2010) have their X-ray pulsations been firmly detected. In this work, we reported our results of X-ray periodicity search of another member in this class — PSR J2021+4026.

PSR J2021+4026 is one of the brightest  $\gamma$ -ray pulsars, which is associated with the supernova remnant (SNR) G78.2+2.1, detected by *Fermi* LAT shortly after its operation (Abdo et al. 2009). The possible association with SNR suggests it is at a distance of  $\sim 1.5$  kpc (Trepl et al. 2010 and references therein). Its proximity makes it as an ideal target for multi-wavelength investigations. Several efforts have been devoted in searching its radio counterpart, no radio pulsar associated with PSR J2021+4026 has been detected so far (Becker et al. 2004; Trepl et al. 2010; Ray et al. 2011).

The timing ephemeris of PSR J2021+4026 has been determined by *Fermi* LAT at different epochs (Abdo et al. 2009a,2010a; Ackermann et al. 2011; Ray et al. 2011; Weisskopf 2011) and no obvious glitch was detected between the epoch of MJD 54680 to MJD 55600. Its observed period and period derivative ( $P = 265$  ms and  $\dot{P} = 5.48 \times 10^{-14}$  s s $^{-1}$ ) imply a spin-down age of  $\sim 77$  kyr, surface dipolar magnetic field strength of  $\sim 4 \times 10^{12}$  G and a spin-down power of  $\sim 10^{35}$  erg s $^{-1}$ . At a distance of 1.5 kpc, its  $\gamma$ -ray conversion efficiency is not dissimilar from that of Geminga (Trepl et al. 2010).

In X-ray regime, a previously unidentified X-ray source, 2XMM J202131.0+402645, has been identified as the promising counterpart of PSR J2021+4026 (Trepl et al. 2010; Weisskopf et al. 2011). This source is found to be the only non-variable X-ray object without any optical/IR counterpart within its  $\gamma$ -ray error circle. Its association with the pulsar is reinforced by the fact that its X-ray position is consistent with the optimal  $\gamma$ -ray timing solution.

For firmly establishing the link between this X-ray source and PSR J2021+4026, a X-ray periodicity search and a detailed spectroscopy is necessary. Nevertheless, this is forbidden by the limited temporal resolution and the small photon statistics of the archival data. In view of this, we have investigated this Geminga-like pulsar with a deep *XMM-Newton* observation. In this Letter, we report the discovery of the X-ray pulsation from PSR J2021+4026. This is the third member of this class with the significant pulsation detected from both X-ray and  $\gamma$ -ray regimes.

## 2. Observations and data analysis

We have observed PSR J2021+4026 with *XMM-Newton* on 2012 April 11 for a total exposure of  $\sim 133$  ks (Obs. ID: 0670590101; PI: Hui). The median satellite bore-sight pointing during this observation is RA=20<sup>h</sup>21<sup>m</sup>30.56<sup>s</sup> Dec=+40°26′46.8″ (J2000), which is the position of 2XMM J202131.0+402645 determined by Trepl et al. (2010). While the MOS1/2 CCDs were operated in full-window mode, PN CCD was operated in small-window mode with a temporal resolution of  $\sim 5.7$  ms, which enables the pulsation search for the first time. With the most updated instrumental calibration, we generated the event lists from the raw data obtained from all EPIC instruments with the tasks *emproc* and *epproc* of the XMM-Newton Science Analysis Software (XMMSAS version 12.0.1). We selected only those events for which the pattern was between 0 – 12 for MOS cameras and 0 – 4 for the PN camera. We also noted that our data have been contaminated by the hard X-ray background flare. After removing all events which are potentially contaminated, the effective exposures are found to be 85 ks, 72 ks and 77 ks for MOS1, MOS2, PN respectively.

### 2.1. Timing analysis

For timing analysis, we utilized solely the PN data for the pulsation search. To determine the source position of 2XMM J202131.0+402645, we have run the source detection with the XMMSAS task *edetect\_chain*. The source can be significantly detected with the signal-to-noise ratio of  $\sim 72\sigma$  at (J2000) R.A.=20<sup>h</sup>21<sup>m</sup>30<sup>s</sup>.53, decl.=+40°26′45″.5 with the uncertainty  $\sim 0''.4$ . We extracted the events within a circular region of a 20″ radius centered at this position, which corresponds to an encircle energy function of  $\sim 76\%$ . Within an energy band of 0.15–12 keV, 3174 counts were available for the timing analysis. With the aid of the task *barycen*, the arrival times of all the selected events were barycentric corrected with the aforementioned X-ray position and the latest JPL DE405 earth ephemeris.

Search around the rotational frequency of PSR J2021+4026 with the method of epoch-folding results in a very significant detection of X-ray pulsation from 2XMM J202131.0+402645. Using either Rayleigh-test (Mardia 1972; Gibson et al. 1982) or  $H$ -test (de Jager et al. 1989; de Jager & Büsching 2010), a significant peak is found at the frequency 3.7689937(9) Hz ( $=0.26532281(6)$  s) with  $Z_1^2 = 126$  and  $H = 133$  respectively. This corresponds to the random probability of  $< 10^{-14}$  (de Jager & Büsching 2010). The quoted uncertainty of our detected frequency is determined by following the method in Leahy et (1987).

Although the ephemeris of PSR J2021+4026 has been determined several times by *Fermi* LAT observations at different epochs (Abdo et al. 2009a,2010a; Ackermann et al. 2011; Ray et al. 2011; Weisskopf 2011), none has covered the epoch of our *XMM-Newton* observation (i.e.  $\sim$ MJD 56028). In order to avoid the uncertainties introduced by extrapolating these timing models to our observation epoch, we derived a  $\gamma$ -ray ephemeris which is contemporaneous with this X-ray observation for comparing the temporal properties in both regimes.

We obtained the *Fermi* LAT data in the energy range of 0.1-300 GeV within a circular region of interest (ROI) with a  $0.8^\circ$  radius from the X-ray position of PSR J2021+4026. In order to achieve a reasonable signal-to-noise ratio and with the influence of the accumulated timing noise minimized, we adopted a data span of  $\sim 1$  year, MJD 55900-56280, which brackets the epoch the *XMM-Newton* observation. For data reduction, the *Fermi* Science Tools v9r23p1 package, available from the *Fermi* Science Support Center<sup>7</sup>, was used. We used Pass 7 data and selected events in the “Source” class (i.e. event class 2) only. In addition, we excluded the events with zenith angles larger than  $100^\circ$  to greatly reduce the contamination by Earth albedo  $\gamma$ -rays. For determining pulse times of arrivals (TOAs), we firstly constructed a template based on the timing model reported by Ray et al. (2011) with the method of Gaussian kernel density estimation. By cross-correlating the template with unbinned geocentered data, which each photon assigned with a phase in accordance with the model reported by Ray et al. (2011), we measured the TOAs from 25 segments of adopted data span.

Using TEMPO2, we fitted the TOAs to a timing model including  $f$ ,  $\dot{f}$ ,  $\ddot{f}$  and  $\ddot{\dot{f}}$ . All spin parameters are allowed to be free with the high order derivatives to account for most of the red noise. For the position, as the short data span does not allow a fit, we fixed it at the X-ray position determined by *Chandra* throughout the analysis (Weisskopf et al. 2011). The results are summarized in Table 1. Since the high order frequency derivatives are dominated by the timing noise, we stress that their values do not reflect the intrinsic

---

<sup>7</sup><http://fermi.gsfc.nasa.gov/ssc/data/analysis/software/>

sic rotational properties of the pulsar. Using the parameters in Tab. 1, the extrapolated  $f$  and  $\dot{f}$  are consistent with the ephemeris at the specified epochs reported by earlier literatures within the statistical uncertainties. According to this local ephemeris, the spin frequency of PSR J2021+4026 at the start of the good time interval (MJD 56028.31153) of our *XMM-Newton* observation is 3.768993208(2) Hz, which is consistent with the detected X-ray pulsation (i.e.  $f = 3.7689937(9)$  Hz).

To compare the X-ray and  $\gamma$ -ray pulse profiles, the photons extracted from our *XMM-Newton* observation and those obtained from *Fermi* within MJD 55910 to 56110 were all folded in accordance with our derived  $\gamma$ -ray ephemeris (i.e. Tab. 1) with the epoch zero at MJD 56028. For further examining the properties of the X-ray pulsation, we performed the energy-resolved timing analysis by dividing the X-ray data into three consecutive bands: 0.15–0.7 keV (soft), 0.7–2 keV (medium) and 2–12 keV (hard). The phase-aligned pulse profiles at different energy ranges are shown in Fig. 1. Apparently, the X-ray pulsation is most significant in the medium band ( $Z_1^2 = 166$ ). In the hard band, there is a very marginal pulse detection of  $Z_1^2 = 17.8$ . However, this corresponds to a much higher random probability of  $\sim 8 \times 10^{-4}$ . In the soft band, there is no conclusive evidence for the pulsation.

There is a recognizable phase offset between the  $\gamma$ -ray and the X-ray profiles (see the left panel in Figure 2). To quantify the phase offset, we computed the cross-correlation between these two phase-aligned light curves. The result is shown in the right panel of Figure 2. The cross-correlation coefficient attains the maximum value at a phase-lag of  $-0.138$ . For estimating the uncertainty of cross-correlation, we used Monte Carlo simulation to obtain the distribution of phase-lag. The simulated X-ray light curves were generated by the original one plus a random series of variates sampled from a Gaussian distribution with a mean of 0 and a standard derivation of  $1\sigma$  corresponds to the errors of observed folded light curve. With 10000 trials, the standard deviation is found to be 0.024 which suggests the aforementioned phase-lag is detected at a confidence level of  $> 5\sigma$ .

## 2.2. Spectral analysis

Apart from detecting the X-ray pulsation, our deep *XMM-Newton* observation is also able to place a tight constraint on the spectral properties of PSR J2021+4026. For spectral analysis, we utilized the data obtained from all three EPIC cameras. With the aid of the XMMSAS task *epatplot*, all the EPIC data are found to be not affected by CCD pileup. We extracted the spectrum of PSR J2021+4026 from circles with a radius of  $20''$  centered at its nominal X-ray position (see §2.1) in MOS1, MOS2 and PN cameras respectively. The background spectra were extracted from the nearby regions in the corresponding CCDs, which

are source-free and with sufficient size to enable a less biased sampling. The response files were generated by the XMM-SAS task *rmfgen* and *arfgen*. After background subtraction, we have 1159 cts collected by EPIC in the energy range of 0.5-10 keV. The photon statistic is  $\sim 4$  times higher than that used in the spectral analysis reported by (Weisskopf et al. 2011). We grouped each spectrum dynamically so as to achieve the same signal-to-noise ratio in each dataset. In order to tightly constrain the spectral parameters, we fitted the data obtained from three cameras simultaneously with XSPEC 12.6.0. For a conservative estimation of uncertainties, the quoted errors of the spectral parameters are  $1\sigma$  for 2 parameter of interest (i.e.  $\Delta\chi^2 = 2.30$  above the minimum) for the single component models and  $1\sigma$  for 4 parameter of interest (i.e.  $\Delta\chi^2 = 4.72$  above the minimum) for the multi-component models.

With the tested single component models, we found that the pulsar spectrum cannot be appropriately described by these simple scenarios. For the absorbed blackbody, it results in a relatively poor goodness-of-fit ( $\chi^2 = 65.33$  for 46 d.o.f.). On the other hand, although the absorbed power-law model results in an acceptable goodness-of-fit ( $\chi^2 = 52.78$  for 46 d.o.f.), it yields a very large photon index ( $\Gamma = 4.4_{-0.5}^{+0.6}$ ) which is far steeper than that expected for a pulsar (cf. Cheng & Zhang 1999). In both of these single component fits, systematic deviations have been noted in the fitting residuals for the energies larger than  $\sim 3$  keV. All these suggest the X-ray emission of PSR J2021+4026 might consist of more than one spectral component.

We proceeded to examine the spectrum with multi-component models. We found that the blackbody plus power-law model (BB+PL) can describe the data reasonably well ( $\chi^2 = 41.55$  for 44 d.o.f.). It yields a column density of  $n_{\text{H}} = (7.0_{-2.7}^{+4.1}) \times 10^{21} \text{ cm}^{-2}$ , a temperature of  $kT = 0.24 \pm 0.06$  keV, a blackbody emitting region with a radius of  $R = 251_{-132}^{+537} d_{1.5}$  m, a photon index of  $\Gamma = 1.2_{-1.2}^{+1.7}$  and a normalization for the power-law component at 1 keV of  $(2.8_{-2.6}^{+14.1}) \times 10^{-6} \text{ photons keV}^{-1} \text{ cm}^{-2} \text{ s}^{-1}$ , where  $d_{1.5}$  represents the distance to PSR J2021+4026 in unit of 1.5 kpc. The best-fit BB+PL model and the residuals for the X-ray spectrum of PSR J2021+4026 are shown in Figure 3. On the other hand, a pure thermal scenario consists of two blackbody components (BB+BB) also results in a comparable goodness-of-fit ( $\chi^2 = 40.19$  for 44 d.o.f.). It yields a set of best-fit parameters of  $n_{\text{H}} = (6.7_{-2.5}^{+3.6}) \times 10^{21} \text{ cm}^{-2}$ ,  $kT_1 = 1.4_{-0.6}^{+1.8}$  keV,  $R_1 = 3.6_{-2.5}^{+6.4} d_{1.5}$  m,  $kT_2 = 0.25 \pm 0.05$  keV and  $R_2 = 223_{-106}^{+320} d_{1.5}$  m. Both of these composite models imply an unabsorbed flux at the level of  $\sim 10^{-13} \text{ ergs cm}^{-2} \text{ s}^{-1}$ .



### 3. Discussion

In this Letter, we report our detection of X-ray pulsation from 2XMM J202131.0+402645. The detected spin frequency is consistent with the  $\gamma$ -ray pulsation of PSR J2021+4026 at the same epoch. This provides a clear evidence that the observed X-rays are indeed from PSR J2021+4026.

The X-ray pulse profile in 0.7-2 keV resembles the modulation resulted from a rotating neutron star with a hot spot on the stellar surface sweeps across our line-of-sight (e.g. Hui & Cheng 2004; Pechenick et al. 1983). This is consistent with the scenario inferred from the phase-averaged spectral analysis which favors a model of blackbody plus power-law or a composite blackbody model. In both of these best-fit models, a blackbody component with a temperature of  $kT \sim 0.25$  keV is required. At a distance of 1.5 kpc, the best-fit blackbody radius is found to be  $\sim 0.2 - 0.3$  km. This is comparable with the canonical size of a polar cap,  $R\sqrt{\frac{R\omega}{c}} \sim 280$  m, where  $R \sim 10$  km represents the typical radius of a neutron star and  $\omega$  is the angular frequency of PSR J2021+4026. According to the outer gap model (Takata, Cheng, & Taam 2012; Cheng & Zhang 1999), the temperature of the polar cap heated by the return current injected by the gap is  $kT \sim 0.3$  keV which is also consistent with the observed value. Furthermore, this spectral component contributes  $> 80\%$  in the observed flux in both BB+PL and BB+BB fits in 0.7-2 keV. All these results point to the thermal nature of the observed X-ray pulsation.

In the BB+PL fit, the non-thermal component with a photon index of  $\Gamma \sim 1.2$  is typical for a canonical pulsar. One possible origin of these non-thermal X-rays is the synchrotron radiation of the relativistic  $e^-/e^+$  from the outer magnetospheric gap (Cheng & Zhang 1999; Takata et al. 2006,2008), which should give rise to a pulsed signal. Despite the best-fit power-law component contributes  $> 90\%$  in the observed flux at the energies  $> 2$  keV, the evidence for the pulsation in the hard band is marginal. This suggested the PL component might be non-pulsed in nature, which can possibly be originated from a pulsar wind nebula (PWN). Indeed, a putative bow-shock associated with PSR J2021+4026 has been marginally resolved by a *Chandra* observation (Weisskopf et al. 2011). It might contribute an steady unpulsed non-thermal X-ray emission as a DC level which can be found in all rotational phases.

On the other hand, the BB+BB model is also able to fit the observed data with a comparable goodness-of-fit. While the low temperature component is consistent with that inferred in the BB+PL fit, it also requires a hotter component with a much smaller emitting area with a radius of few meters. This might be a phenomenological two-steps adaptation for a wider temperature distribution of the hot polar cap with the hotter component de-

scribing the peak of the distribution. The marginal detection of X-ray pulsation in the hard band might be originated from the modulation of this component. However, the inferred temperature,  $\sim 2 \times 10^7$  K, is higher than that expected from the heating by the back flow current from the outer gap (Cheng & Zhang 1999) unless the surface multipolar magnetic field is strong enough to reduce the pure dipolar cap area.

Comparing the phase-aligned X-ray and  $\gamma$ -ray light curves (Fig. 1), their pulse morphologies are clearly different where the  $\gamma$ -ray profile is narrower and contains at least two peaks. In cross-correlating these two profiles, the cross-correlation coefficient is found to attain the maximum value of  $\sim 0.67$  at a phase lag of  $\sim -0.14$  as shown in the right panel of Fig. 2. This clearly indicates that the observed X-rays and  $\gamma$ -rays are originated from different sites. By comparing these observed results with the model predictions, the pulsar emission geometry (e.g. magnetic inclination angle, viewing angle) can be constrained. In the previous study, Trepl et al. (2010) has modelled the  $\gamma$ -ray pulse profile of PSR J2021+4026 in the context of the outer gap model. Nevertheless, due to the lack of pulses detected in radio and any other wavelength at that time, there was an uncertainty in determining which peak is leading (see Fig. 13 & 14 in Trepl et al. 2010). With our detection of X-ray pulsation, such ambiguity can now be resolved and thus the theoretical investigation of this pulsar can be re-visited.

This research has made use of the data obtained through the *Fermi* Science Support Center Online Service, provided by the NASA/Goddard Space Flight Center. The work is partially supported by the National Science Council through grants NSC 101-2112-M-039-001-MY3. C.Y.H. and K.A.S. are supported by the National Research Foundation of Korea through grant 2011-0023383. C.P.H. and Y.C. are supported by the National Science Council of Taiwan through the grant NSC 101-2112-M-008-010. R.H.H.H. acknowledges support from the National Science Council through grants NSC 100-2628-M-007-002-MY3 and NSC 100-2923-M-007-001-MY3. J.T. and K.S.C. are supported by a GRF grant of HK Government under HKU700911P.

## REFERENCES

- Abdo, A. A., et al. 2008, *Science*, 322, 1218  
 Abdo, A. A., et al. 2009a, *Science*, 325, 840  
 Abdo, A. A., et al. *ApJS*, 183, 46  
 Abdo, A. A., et al. *ApJ*, 712, 1209



- Abdo, A. A., et al. ApJ, 711, 64
- Abdo, A. A., et al. ApJS, 187, 460
- Ackermann, M., et al. 2011, ApJ, 726, 35
- Becker, W., et al. 2004, ApJ, 615, 897
- Bertsch, D. L., et al. 1992, Nature, 357, 306
- Camilo, F., et al. 2009, ApJ, 705, 1
- Caraveo, P. A., De Luca, A., Marelli, M., Bignami, G. F., Ray, P. S., Saz Parkinson, P. M., & Kanbach, G. 2010, ApJ, 725, L6
- Cheng, K. S., & Zhang, L. 1999, ApJ, 515, 337
- de Jager, O. C., & Büsching, I. 2010, A&A, 517, L9
- de Jager, O. C., Raubenheimer, B. C., & Swanepoel, J. W. H. 1989, A&A, 221, 180
- de Jager, O. C., Raubenheimer, B. C., & Swanepoel, J. W. H. 1986, A&A, 170, 187
- Gibson, A. I., Harrison, A. B., Kirkman, I. W., Lotts, A. P., Macrae, J. H., Orford, K. J., Turver, K. E., & Walmsley, M. 1982, Nature, 296, 833
- Halpern, J. P., & Holt, S. S. 1992, Nature, 357, 222
- Hui, C. Y., & Cheng, K. S. 2004, ApJ, 608, 935
- Kerr, M. 2011, ApJ, 732, 38
- Leahy, D. A. 1987, A&A, 180, 275
- Lin, L. C. C., Huang, R. H. H., Takata, J., Hwang, C. Y., Kong, A. K. H., & Hui, C. Y. 2010, ApJ, 725, L1
- Mardia, K.V. 1972, Statistics of direction data, Academic Press, New York
- Pechenick, K. R., Ftaclas, C., & Cohen, J. M. 1983, ApJ, 274, 846
- Pletsch, H. J. 2011, Phys. Rev. D, 83, 122003
- Pletsch, H. J., et al. 2012a, ApJ, 744, 105
- Pletsch, H. J., et al. 2012b, ApJ, 755, L20

Ray, P. S., et al. 2011, ApJS, 194, 17

Saz Parkinson, P. M., et al. 2010, ApJ, 725, 571

Takata, J., Cheng, K. S., & Taam, R. E. 2012, ApJ, 745, 100

Takata, J., Chang, H., & Shibata, S. 2008, MNRAS, 386, 748

Takata, J., Shibata, S., Hirovani, K., & Chang, H.-K. 2006, MNRAS, 366, 1310

Trepl, L., Hui, C. Y., Cheng, K. S., Takata, J., Wang, Y., Liu, Z. Y., & Wang, N. 2010, MNRAS, 405, 1339

Weisskopf, M. C., et al. 2011, ApJ, 743, 74

Table 1: Local ephemeris of PSR J2021+4026 derived from LAT data which brackets the *XMM-Newton* observation on MJD 56028. The numbers in parentheses denote errors in the last digit.

Parameter	
Pulsar name .....	PSR J2021+4026
Valid MJD range .....	55908—56274
Right ascension, $\alpha$ .....	20:21:30.733
Declination, $\delta$ .....	+40:26:46.04
Pulse frequency, $f$ ( $\text{s}^{-1}$ ) .....	3.768995206(2)
First derivative of pulse frequency, $\dot{f}$ ( $\text{s}^{-2}$ ) ..	$-8.166(3) \times 10^{-13}$
second derivative of pulse frequency, $\ddot{f}$ ( $\text{s}^{-3}$ ) ..	$-2(1) \times 10^{-22}$
Third derivative of pulse frequency, $\dddot{f}$ ( $\text{s}^{-4}$ ) ..	$1(2) \times 10^{-29}$
Epoch of frequency determination (MJD) ..	56000
Solar system ephemeris model .....	DE405
Time system .....	TDB

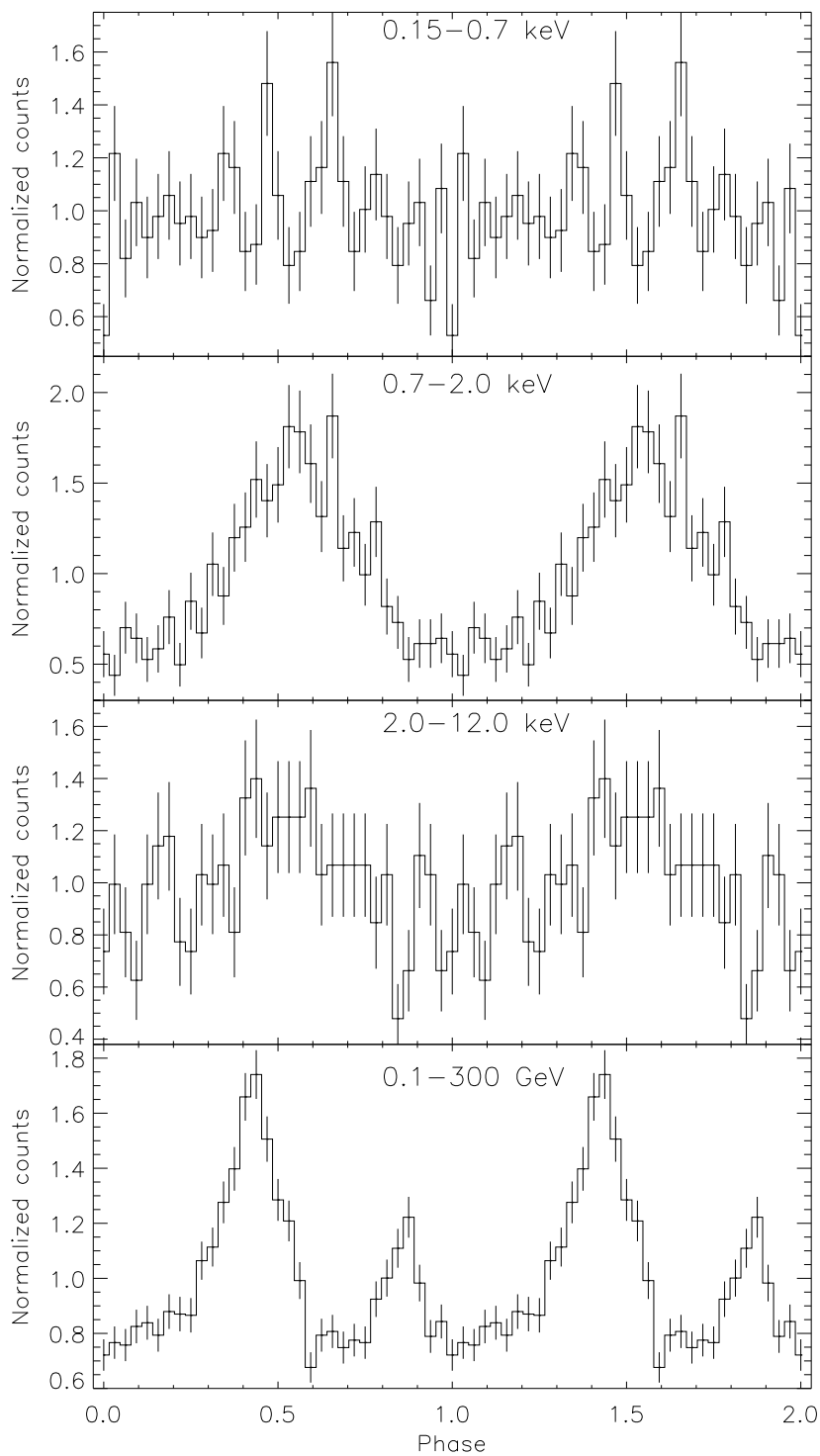


Fig. 1.— Folded light curves of PSR J2021+4026 in different energy ranges. Each panel shows the pulse profile of 32 bins in the energy band specified in the legend. All the light curves were folded with the timing parameters at the epoch/phase zero of MJD 56028 derived from Table 1.

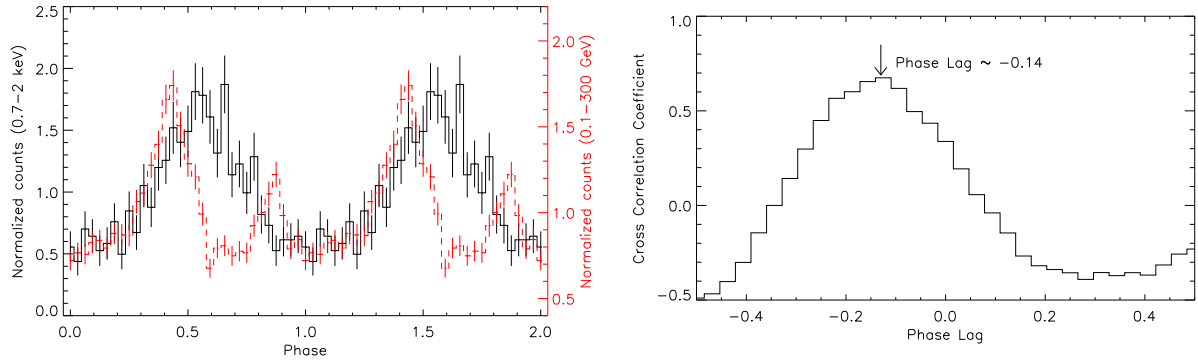


Fig. 2.— Correlation of the X-ray and  $\gamma$ -ray pulsations. *Left panel:* The light curves of PSR J2021+4026 in X-ray and  $\gamma$ -ray bands both folded at the epoch zero of MJD 56028 with 32 bins using the same ephemeris reported in this letter. The pulse profiles in 0.7–2 keV and 0.1–300 GeV are illustrated as solid line and dashed line respectively. *Right panel:* Cross-correlation of the X-ray and  $\gamma$ -ray pulse profiles is shown. The coefficient has a maximum value at a phase lag of -0.14.

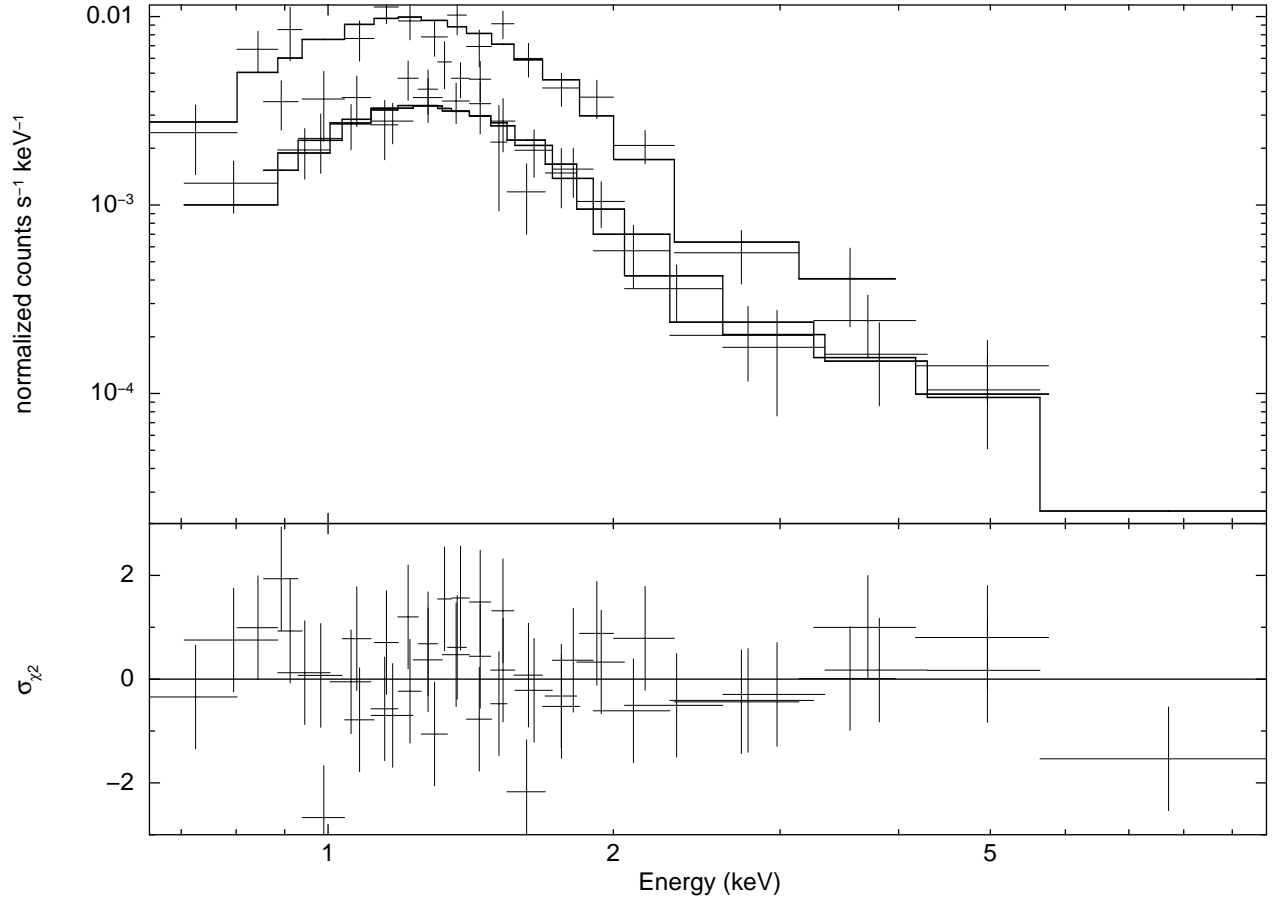


Fig. 3.— The phase-averaged energy spectrum of PSR J2021+4026 in 0.5–10 keV. The X-ray emission from the position of PSR J2021+4026 as observed with the PN (upper spectrum) and MOS1/2 detectors (lower spectra) are simultaneously fitted to an absorbed blackbody plus power-law model (*upper panel*) and contributions to the  $\chi^2$  fit statistic (*lower panel*).